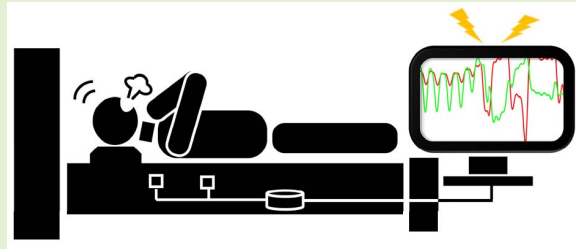


Furniture-Integrated Respiration Sensors by Notched Transmission Lines

Zijing Zhang^{ID}, Pragya Sharma^{ID}, Member, IEEE, Jianlin Zhou^{ID}, Xiaonan Hui^{ID}, Member, IEEE, and Edwin C. Kan, Senior Member, IEEE

Abstract—Non-invasive respiration sensors integrated into furniture can be invisible to the user and greatly enhance comfort and convenience to facilitate many applications. Current sensors often require user cooperation or fitting, which discourages frequent usage. We present a new respiration sensor integrated into a bed or a chair by modifying a radio-frequency (RF) coaxial cable structure with a designed notch. The lung motion is coupled to the electromagnetic leakage at the notch through near-field coherent sensing (NCS). The sensors, covered with fabrics and positioned under the abdomen and thorax, can capture the respiratory waveforms and derive the breath rate. The heart rate can also be evaluated in the same setup with proper filtering. The sensor design can tolerate large position variation to accommodate user uncertainties. Various voluntary exercises of normal, deep, fast, held and blocked breathing were measured under different postures of supine, recumbent and sitting by the carrier frequency range between 900MHz and 2.4GHz. The breath rate from 10 participants compare well with the synchronous commercial chest-belt sensors in all breathing routines.



Index Terms—Microwave sensors, respiration sensors, apnea detection.

I. INTRODUCTION

MONITORING respiration dynamics has many applications [1], including in wellness evaluation and diagnosis of respiratory disorders such as asthma [2], coughing, dyspnea, and chronic obstructive pulmonary diseases (COPD) [3]. It is also valuable for prognostic assessment of prevalent sleep disorders including central sleep apnea (CSA) and obstructive sleep apnea (OSA) [4]. Irregular breathing patterns can be an early indicator of cardiac arrest [5] and acute myocardial infarction [6]. Besides clinical applications, respiration monitoring can also be a useful gauge of cognitive load [7], emotional stress, and physical efforts during sports and exercises [8].

Manuscript received August 4, 2020; revised September 29, 2020; accepted October 2, 2020. Date of publication October 6, 2020; date of current version January 15, 2021. This work was supported in part by the Department of Defense of United States through the Office of the Congressionally Directed Medical Research Programs (CDMRP) Discovery Award PR-182496 and in part by the National Institute of Health (NIH) under Grant DA049566-01A1. The associate editor coordinating the review of this article and approving it for publication was Dr. Sanket Goel. (*Corresponding author: Zijing Zhang.*)

The authors are with the School of Electrical and Computer Engineering, Cornell University, Ithaca, NY 14853 USA (e-mail: zz587@cornell.edu; ps847@cornell.edu; jz899@cornell.edu; xh273@cornell.edu; eck5@cornell.edu).

This article has supplementary downloadable material available at <https://ieeexplore.ieee.org>, provided by the authors.

Digital Object Identifier 10.1109/JSEN.2020.3028970

Current methods to monitor respiration efforts include spirometry [9], nasal airflow probe [10], capnography [11], strain gauges [12], respiratory inductance plethysmography (RIP) [13], pulse oximetry [14], skin strain sensors [15], optical and far-field RF sensing [16], [17], and ballistocardiogram (BCG) [18]. Spirometry measures the volume and speed of inhaled and exhaled air by the lung, but requires attentive user participation. Nasal airflow probes utilize mouthpieces or face-masks, which are cumbersome and disruptive to the normal breathing patterns. Capnography needs similar conspicuous mouth or nasal cannula. Strain gauges and RIP by chest belts can measure the chest and abdominal wall movement during respiration, but the belt tension is required to capture the full breathing cycle which causes discomfort. The skin strain sensor involves tight skin contact which is also uncomfortable. Pulse oximetry monitors the oxygen saturation (SpO₂) and offers mixed observation of respiration and circulation. Optical and RF sensing methods require the user to be stationary and the reader to be in a direct line-of-sight (LoS) to the front torso. BCG-based sensors often assume the user body weight as the quiescent point of operation, and can only be installed under the bed but not to the chair. Posture variation and movement on bed are problematic as well.

Transmission-line sensors have been used in biological and chemical sensing as well as health monitoring. A splitter-combiner structure can measure minute dielectric property

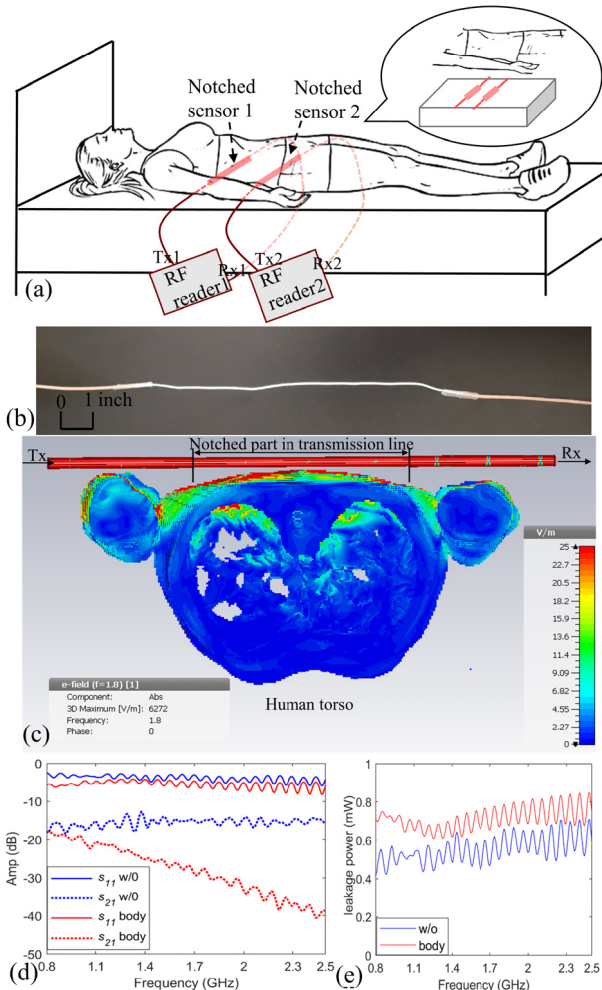


Fig. 1. Notched-cable respiration sensor setup: (a) System schematic with bed integration; (b) A photo of the notched cable; (c) Cross section of the CST simulation of a human torso with the NCS frequency at 0.9GHz; (d) Measured S_{11} and S_{21} results in 0.8 – 2.5 GHz after de-embedding. (e) Estimated leakage power from the notched sensor with 1mW input.

changes in the near-field region [19]. A coplanar waveguide loaded with symmetric resonators can measure angular motion [20] and dielectric properties [21]. A resonator coupled to a transmission line was used to estimate glucose concentration [22]. The sensing modality is typically the variation of the resonance frequency, phase, and/or quality factor. The transmission-line structure is highly sensitive to small motion and composition changes, and hence has been rarely applied to the large motion of respiration. The highest sensitivity may not be favorable here, as tolerance to user variation and the capture of the full waveforms are also important in practical applications.

The notched transmission-line sensor proposed in this article is adapted from the previous antenna-based near-field coherent sensing (NCS) [23], as shown in Fig. 1. In the near-field region, the dielectric boundary movement by internal organs and body parts will couple to the leaked electromagnetic (EM) energy from the notched part of the transmission line, and hence affect the signals at the transmitting (S_{11}) and receiving (S_{21}) ends. To connect to the sensing notch with high

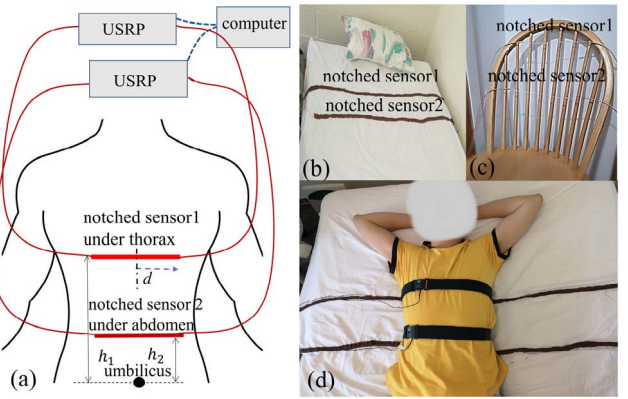


Fig. 2. Experimental setup of the notched sensors: (a) Sensor position variation with respect to the user body; (b) Bed integrated and (c) chair integrated setup; (d) A photo with the participant lying on the bed-integrated sensor and wearing commercial torso belts for benchmark.

ambient isolation, we opt to use a miniature coaxial RF cable, as shown in Fig. 1(b), which is more feasible than the coplanar or slotline waveguides. The metal shield of the middle part is removed to allow the EM energy coupled into the nearby user body. Simulation by CST Microwave Studio [24] with the notched sensor on the human torso is shown in Fig. 1(c). The simplified torso model only includes the sweatshirt, skin, muscle, body fat, bones and lungs to save computational time. RF signals were emitted from the transmitter (Tx) and propagated down the transmission line. The EM leakage from the notched structure was coupled into the human body, and finally received by the receiver (Rx). We can clearly observe that the electric field was strongly coupled into the layers of skin, fat, muscle, and lungs. More details of the simulation setup are shown in supplementary Fig. 1.

The notch length $L = 9$ in is designed to accommodate the position uncertainties for different users on beds and chairs. As shown in Fig. 2, the notched cable was sewn on the bedsheets for the bed setup, while it was fixed at the back of the chair for the chair setup. Intermediate layers of thin fabric, plastic protector and foam can be added for comfort and aesthetic with little influence on performance. In comparison with either far-field [17] or near-field [25], [26] effects of the sensing antenna structure, the present design can operate in a much broader bandwidth with a given hardware as indicated by the measured S_{21} in Fig. 1(d) and by the simulated S_{21} in Supplementary Fig. 1. As no RF radiation is intended and the Rx power can be anywhere between -5 dB to -50 dB lower than the Tx power, the Bode-Fano limit on percentage bandwidth and impedance match [27] and spectral regulation are much more relaxed. Also, in contrast to wearable NCS sensors [23], [25], [26], the user may not need to tend to the sensor at all, which greatly reduces the comfort and conspicuousness concerns. We further demonstrated the capability of accurate respiration monitoring under various postures, including supine, recumbent and sitting. Different respiratory routines including voluntary deep, fast and tidal breathing, as well as breath holding and airway blockage exercises, can be identified accurately. Our sensor can also retrieve

the heart rate in one setup, although the cardio waveform is clearest during breath holding with reduced interference by the large respiratory motion. We benchmarked our sensor against the chest-belt respiration measurements with high consistency. The validity of our system has been confirmed on 10 healthy adults.

II. EXPERIMENTAL SETUP AND SIGNAL PROCESSING

A. Notched Sensor Configuration

To demonstrate the broadband operability, continuous-wave (CW) signals between 0.8 and 2.5 GHz were tested by the network analyzer (Keysight E5063A) in the bed setup. The EM energy emitted from Port 1 will partially leak out from the notch and couple to the surface and internal body motion of breathing and heartbeats, which will change the signal at Port 2 as represented by the scattering parameter S_{21} . Some of the traveling wave will be reflected back to Tx, and can be potentially evaluated as S_{11} or standing-wave ratios, as shown in Fig. 1(d) when the human body was lying on the bed (red line) and when the bed is empty (blue line). The RF carrier power is set at 0 dBm, and the leakage power from the notched structure can be estimated by $(1 - |S_{21}|^2 - |S_{11}|^2) \times 1\text{mW}$ after de-embedding the cable loss, as shown in Fig. 1(e).

Two sets of the notched-cable sensors underneath the thorax and abdomen regions can capture the separate motion during breathing. Multiplexing by frequency or chip codes is optional, as the cross coupling of the thorax and abdomen sensors is weak due to small far-field radiation. Two software-defined radios (SDR) by National Instrument Ettus B200mini were connected to two notched cables and then interfaced with the host computer through USB (Universal Serial Bus). Alternatively, one SDR by the two ports of Ettus B210 can be employed. When the participant is lying on the bed or sitting on the chair, the centers of the sensor notches have a horizontal distance d to the mediastinum, and the vertical distances h_1 and h_2 to the umbilicus for the thorax and abdomen sensors, as shown in Fig. 2(a). Figs. 2(b)(c) are the photos for the bed- and chair-integrated setups. In realistic deployment, we can also sew the sensor beneath the bed sheet and protective layers to facilitate routine changes, disinfection, and aesthetic design. For verification, we benchmarked the NCS results with the BIOPAC tension-belt sensors (BIOPAC Systems, Goleta, CA). Two torso belts, SS5LB and PTM SS11LB, were placed at thorax and abdomen, with the vertical positions right above the NCS sensors. A photo is shown in Fig. 2(d). The torso belts can measure the change in local tension due to the geometrical change during respiration. BIOPAC data are down-sampled to 500Hz. The synchronization between NCS and BIOPAC is achieved by buffering the NCS and BIOPAC data at approximately the same time within a few milliseconds.

In the SDR Tx signal chain, the digital baseband goes through the digital-to-analog converter (DAC) and is then mixed with the carrier frequency f_{RF} . The RF signal from the notched structure is coupled into internal body motion in the near-field, received by Rx, and then demodulated and sampled by the analog-to-digital converter (ADC) to retrieve the baseband. Together with a baseband tone f_{BB} in the quadrature scheme, the NCS vital-sign signal is represented

by the amplitude modulation on the quadrature signal as

$$NCS(t) = \sqrt{I_{Rx}(t)^2 + Q_{Rx}(t)^2} \quad (1)$$

$$I_{Rx}(t) = A(t)\cos(2\pi f_{BB}t + \theta_0) \quad (2)$$

$$Q_{Rx}(t) = A(t)\sin(2\pi f_{BB}t + \theta_0) \quad (3)$$

where θ_0 is the phase offset accumulated from the Tx-Rx signal chains. The baseband frequency is set at $f_{BB} = 51\text{ kHz}$ for B200mini. When B210 is used for both channels, the two basebands are set at $f_{BB1} = 355\text{ kHz}$ and $f_{BB2} = 440\text{ kHz}$. f_{RF} is selected to be at one of 900MHz, 1.8GHz and 2.4GHz. As the respiration waveform is a low-frequency analog signal, we chose the superheterodyne scheme of converting the frequency twice by f_{BB} and f_{RF} to minimize the effects of the Flicker noise in f_{RF} local oscillators (LO) and to implement subcarrier multiplexing from f_{BB1} and f_{BB2} when needed. We have varied a few f_{BB} in supplementary Fig. 2 to substantiate our choices. The data converter has a sampling frequency of 1M samples per second (Sps) to enable the digital baseband processing, which is performed by the host computer. The demodulated respiration waveform is further down-sampled to 500 Sps, the same as the BIOPAC data. The allowable broad choice of f_{RF} is not only a unique feature over the antenna-based NCS approach, but can also facilitate system tuning after furniture integration so that f_{RF} can yield strong coupling to the user body with higher ambient tolerance.

B. Breath Rate (BR) Estimation

For estimation of the breath rate (BR), the waveform was first bandpass-filtered from 0.05Hz to 1Hz to remove the DC drift and high-frequency noises by post-processing in MATLAB. For peak detection to identify the inhalation and exhalation periods, we utilized the moving average-crossing algorithm [28], which is suitable to process broad range of varying frequencies, as we expect BR ranging from nearly 5 breaths per minute (BPM) to 40 BPM. A moving-average curve is first calculated at each time point in a given window length, which is around one respiration cycle and will be constantly updated. The points when the moving average curve crosses the original signal are marked as up-crossing points for positive slopes in the original signal or down-crossing points for negative. Local maximum is labelled as the maximal point between two up-down crossing points, and local minimum as the minimal point between two down-up crossing points. BR is finally calculated by counting the number of detected breathing cycles over a window size of 15s. One breathing cycle includes an inhalation peak (maximum) and the trailing exhalation (minimum) peak. The number of cycles is calculated as the number of inhalation peaks minus 1, and the total period is between the two adjacent inhalation peaks.

C. Signal Quality and Bit Depth

The signal quality can be assessed by the acquired bit depth of the respiratory waveform, which represents the signal resolution and provides insights into the amount of RF energy

coupled inside the internal organ. In this article, we define the bit depth of the signal quality Q as,

$$Q = \log_2 \frac{NCS_{pp}}{NCS_{DC}} + N - 1 \quad (4)$$

where NCS_{pp} is the peak-to-peak value in the quadrature-demodulated amplitude, NCS_{DC} is the DC amplitude at the local point, and N is the number of bits in ADC. NCS_{pp} can be retrieved by the peak detection algorithm, and NCS_{DC} can be obtained by the DC signal amplitude before filtering. Q has the meaning of the number of significant bits in the NCS signal. As the respiration waveform is cyclic around an equilibrium point, the larger the signal strength, the more bit depth can be retrieved by ADC, and hence the higher the signal resolution and the less quantization noises.

Signal-to-noise ratio (SNR) is another important parameter to evaluate the hardware system setup. We estimate SNR during the normal breathing period when BR is roughly constant. The fundamental breathing frequency can be determined from the largest nonzero spectral component. The 3-dB bandwidth of the breathing frequency includes all adjacent frequency components that decrease monotonically away from the maximum. The noise level is estimated by using the total power outside the 3-dB regions of the fundamental breathing frequency, its harmonics and the DC component.

Signal quality and SNR under different postures, breathing patterns, positions and frequencies can give guidance to the hardware design and signal processing to accommodate inevitable user variations in realistic applications. Larger signal quality often indicates higher SNR from the NCS signal strength, but in a less controlled ambient, SNR still offers additional useful information on ambient noises.

D. Isovolumetric Breathing Detection During Airway Blockage

One of the most common apneas is the obstructive sleep apnea (OSA). OSA often occurs when the throat muscles intermittently relax and block the airway during sleep. As the lung volume will remain nearly constant during OSA, the thorax and abdomen move asynchronously to generate a paradoxical motion. During our experiments, this symptom was simulated by the isovolumetric breathing exercise. By blocking the airway voluntarily with a nose pinch, abdomen contraction was performed with paradoxical expansion of the thorax and vice versa. To detect this paradoxical movement, we can use the slope-product of thorax and abdomen waveforms, which will be negative during the occurrence of isovolumetric breathing [29]. We use the $\tanh()$ function to rescale the slope-product to $[-1,1]$ with a moving average over a 3s window [29].

III. EXPERIMENTAL RESULTS

A. Benchmark With BIOPAC Tension Belts

The NCS notched-cable sensor was benchmarked against the reference BIOPAC tension-belt sensors. Notice that both sensors can have errors in respiration monitoring, but due

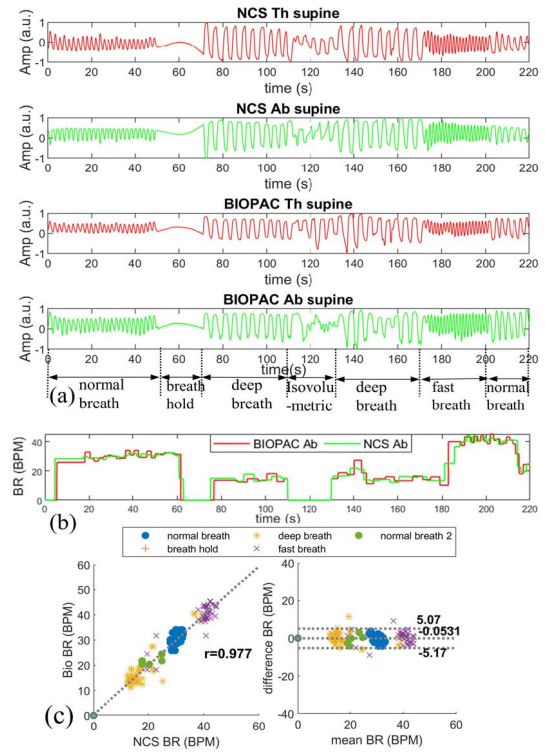


Fig. 3. Respiration monitoring in the supine posture with $f_{RF} = 900\text{MHz}$: (a) NCS and BIOPAC amplitude waveforms in thorax and abdomen during the whole breathing protocol. (b) Th breath rate (BR) calculated from NCS (green) and BIOPAC (red). (c) Correlation and agreement between NCS and BIOPAC BR data. Left: The scatter plot with denoted Pearson's correlation coefficient. Right: The Bland-Altman plot showing the mean difference m at the center dotted line and the corresponding limits of agreement (LoA) at the upper and lower dotted lines given by $m \pm 1.96\sigma$.

to the different signal transduction, the errors from the two methods should be reasonably uncorrelated. Vertical positions of the sensors are recorded by the distance to the umbilicus with $h_{1NCS} = 8.5$ in, $h_{2NCS} = 2.5$ in, $h_{1BIOPAC} = 9$ in, and $h_{2BIOPAC} = 3.5$ in. The breathing protocol in each posture has a length of 220 s, including 0 – 50 s: normal tidal breathing; 50 – 70 s: breath hold; 70 – 110 s: deep breathing; 110 – 130 s: isovolumetric exercise; 130 – 170 s deep breathing; 170 – 200 s: fast breathing; 200 – 220 s: normal breathing.

Fig. 3(a) shows the normalized NCS and BIOPAC amplitude waveforms in thorax and abdomen with the supine position on bed during the whole protocol. Both NCS and BIOPAC data can distinguish different breathing patterns clearly and show a good agreement. Fig. 3(b) shows BR calculated from NCS and BIOPAC abdomen amplitude, as the geometrical change from diaphragm and abdomen is higher than that of thorax during respiration. When the negative slope product was detected during the isovolumetric exercise, BR was truncated to 0. BR estimation matched well with the breathing patterns, but a delay in time was observed due to the chosen 15-s epoch for BR calculation. Fig. 3(c) shows the correlation between NCS and BIOPAC. The BR data was preprocessed by getting rid of the outliers that were three standard deviations

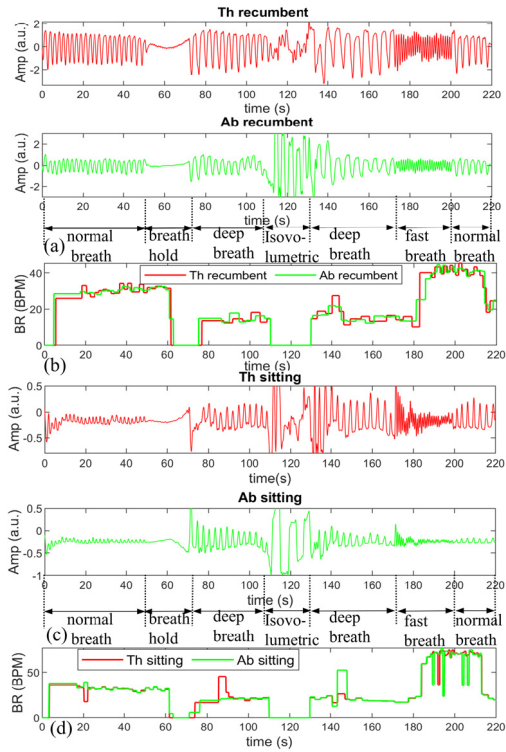


Fig. 4. Respiration monitoring in the recumbent and sitting postures: (a) Respiratory waveforms from thorax and abdomen NCS sensors in the recumbent posture on bed with $f_{RF} = 2.4\text{GHz}$. (b) BR estimated from (a). (c) Respiratory waveforms from thorax and abdomen NCS sensors in the sitting posture on chair with $f_{RF} = 1.8\text{GHz}$. (d) BR estimated from (c).

further away from the mean. The outliers only occurred at the beginning or ending of a specific breathing pattern due to the instability of a transition. These outliers were not included for correlation calculation. High correlation with a Pearson coefficient $r = 0.977$ is achieved. As the two sensors have uncorrelated errors, correlation is one of the possible indicators for inter-sensor consistency and overall BR accuracy. The Bland-Altman plot on the right presents the agreement by the mean (m) and limits of agreement (LoA). The X axis is the average of the two data, and the Y axis is the difference. The mean difference is $m = -0.306 \text{ BPM}$, as shown in the middle dotted line. LoA within which 95% of the differences is estimated by $m \pm 1.96\sigma$, assuming a normal distribution. Low m and narrow LoA indicate that the errors in NCS and BIOPAC are uncorrelated and small. In Fig. 3, f_{RF} is set at 900MHz. Results with f_{RF} at 1.8GHz and 2.4GHz are shown in supplementary Fig. 3.

B. Posture Variation

The NCS notched-cable sensor can be applied to different postures, including supine and recumbent on bed, and sitting on chair, which can be readily adapted for sleep study, driver seat and waiting-room chairs. In Fig. 4, we demonstrated the results from the recumbent and sitting postures. The breathing protocol was the same as in Fig. 3. Waveforms were based on the normalized NCS amplitude after bandpass filtering of 0.05 - 1 Hz. For the recumbent posture in Figs. 4 (a)(b),

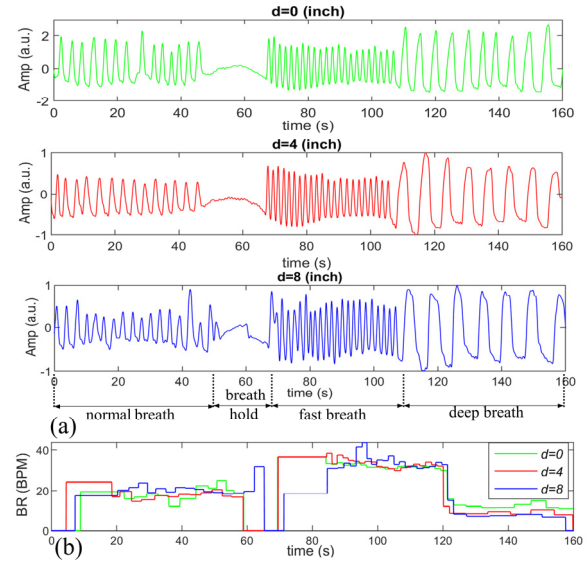


Fig. 5. (a) Respiration waveforms with horizontal shift of $d = 0, 4, 8$ inches for the abdomen sensor in the supine posture on bed. (b) BR estimated from the respiration waveforms for $d = 0$ (green); $d = 4$ in (red); $d = 8$ in (blue).

$h_1 = 8.5$ inches, $h_2 = 2.5$ inches, and $f_{RF} = 2.4\text{GHz}$. For the sitting posture in Figs. 4 (c)(d), $h_1 = 9.5$ inches, $h_2 = 2$ inches, and $f_{RF} = 1.8\text{GHz}$. BR during the 20-s isovolumetric exercise was also truncated to zero once the negative slope product was detected. Data quality from the recumbent posture is sufficient for BR estimation, but slightly worse than that in the supine posture, which is likely due to less interaction area with the RF signal. As can be observed in the first 50-s normal breathing with reduced magnitude, the sitting posture suffered more noises and showed less clear breathing pattern. This may be due to possible slouching, which will seriously affect the abdomen waveforms. However, various breathing patterns can still be identified in Figs. 4 (a)(c), including tidal breathing, breath hold, deep breathing, and fast breathing. BR in Figs. 4 (b)(d) shows a good match between the thorax and abdomen sensors. Test results from other f_{RF} are shown in supplementary Fig. 4.

C. Position Variation

One of the requirements for furniture-integrated sensors different from the wearable ones is the large placement tolerance to accommodate user variation in size and position. We tested the sensor performance when a horizontal shift d was introduced in the supine posture, which can commonly happen in realistic conditions. We confirmed that our notched cable system can tolerate up to $d = 8$ in, which should be sufficient in consideration of user uncertainties. The participants in our test have an average waist width around 12 in. To speed up the study, the breathing protocol was shortened to 160s, including 0 – 50 s: normal breathing; 50 – 70 s: breath hold; 70 – 110 s: fast breathing; 110 – 160 s: deep breathing. f_{RF} was set to 2.4GHz. Fig. 5(a) shows the normalized NCS waveforms after filtering with the horizontal shift of $d = 0, 4, 8$ in from the abdomen sensor. Different respiration patterns can

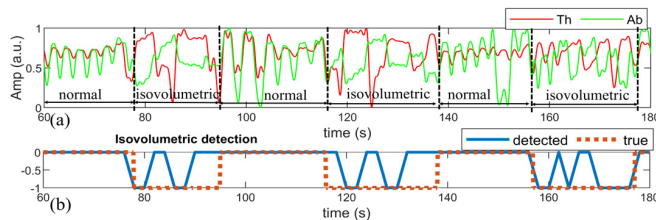


Fig. 6. Isovolumetric detection: (a) Respiration waveforms from thorax (red line) and abdomen (green line) sensors during three isovolumetric breathing exercises. (b) Detection by the slope-product method: The blue solid line by the NCS sensor and the orange dotted line from protocol annotation, where -1 indicates detection.

still be clearly identified and the transition remained evident. Fig. 5(b) shows BR estimated from the respiration waveforms, where normal BR is around 20 BPM, fast BR around 35 BPM, and deep BR around 10 BPM. For $d = 8$ in, BR around the breath hold period is not as accurate as $d = 0$ and 4 in due to the reduced signal quality. Position variation results from other f_{RF} are shown in supplementary Fig. 5. We also tested the vertical position variation of $h_1 = 1, 2.5, 4$ in for abdomen sensor with the same protocol. Results are shown in supplementary Fig. 6.

D. Isovolumetric Exercises

The isovolumetric exercise was represented by paradoxical motion between thorax and abdomen. The 270-s breathing protocol was customized to increase the total period of isovolumetric motion including 0 – 40 s: normal breathing; 40 – 60 s: breath hold; 60 – 80 s normal breathing. Four isovolumetric exercises were then performed roughly during 80 – 100 s; 120 – 140 s; 160 – 180 s; 200 – 220 s, with normal breathing in between and afterwards.

Fig. 6(a) shows an example of the waveforms from thorax and abdomen NCS signals during three isovolumetric cycles. f_{RF} was set to 900 MHz. As the waveforms indicate, in normal breathing periods, the thorax and abdomen moved synchronously; in the isovolumetric periods, the two motions were paradoxical to each other. The slope-product method was implemented in Fig. 6(b), where -1 indicates positive detection of isovolumetric motion and 0 indicates no occurrence. The annotated instruction to perform the isovolumetric exercise is shown as the orange dotted line and the NCS detection result as the blue solid line.

Isovolumetric exercises can be missed or falsely detected by NCS or BIOPAC. False statistics against the user instruction are summarized for 10 volunteers in Table I. NCS could detect a large portion of airway blockage successfully and performed slightly better than BIOPAC. Possible reasons for erroneous detection include: 1) The notched sensors couple into the motion of associated muscles whose movement during airway blockage can be complex instead of merely paradoxical; 2) Some participants had difficulty performing the isovolumetric exercise during airway blockage, or had introduced body motion artifacts during their attempts; 3) The thorax sensor was too low in position and had coupled in part of the abdomen motion as well.

TABLE I
CONFUSION MATRICES OF ISOVOLUMETRIC BREATHING DETECTION
DURING AIRWAY BLOCKAGE BY NCS AND BIOPAC

		NCS	
Total number of epochs in 10 participants: 180		Detection	
Airway blockage instruction	Positive	16	4
	Negative	10	150
accuracy		0.92	
sensitivity		0.8	
		BIOPAC	
Total number of epochs in 10 participants: 180		Detection	
Airway blockage instruction	Positive	11	9
	Negative	11	149
accuracy		0.89	
sensitivity		0.65	

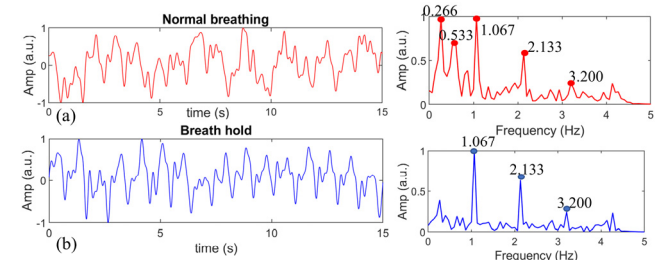


Fig. 7. (a) Left: The heartbeat time-domain waveforms from the thorax sensor during normal breathing. Right: The corresponding spectrum with three HR peaks and two BR peaks indicated by the annotation above. (b) Left: The heartbeat waveforms during breath hold. Right: The corresponding spectrum with three peaks.

E. Heart Rate (HR) Detection

With the same setup, the thorax NCS sensor can also retrieve the heart rate (HR) with reasonable accuracy. The test protocol was further simplified to normal breathing of 15 s and breath hold of 15 s, the latter of which had clearer heartbeat signals due to the lack of respiration interferences. The signal was first filtered by a bandpass filter between 0.1 – 5 Hz to remove the DC component and high-frequency noise. Fig. 7(a) shows the NCS waveform during normal breathing in time (left) and frequency (right) domains. Fig. 7(b) shows the breath-hold counterpart. The waveform has a typical characteristic of a main peak and a small recoil. HR can be observed as the fundamental, second and third harmonics in the spectrum. BR at 0.266 Hz and its harmonics can also be observed in Fig. 7(a). f_{RF} was set to 1.8 GHz, but HR can be retrieved at other f_{RF} as well, which is shown in Supplementary Fig. 7.

F. Signal Quality and SNR

We have calculated the signal quality Q for different scenarios in Fig. 8. The means and standard deviations of Q in Fig. 8 are shown in Supplementary Table II. First, the breathing patterns over time can cause variation in Q . For the same setup, the deep breathing usually has the highest Q , and the breath hold the lowest. The position variation of $d = 0, 4, 8$ in is shown in Fig. 8(a) with $f_{RF} = 2.4$ GHz. When d becomes larger, most often Q decreases. We compare the thorax and

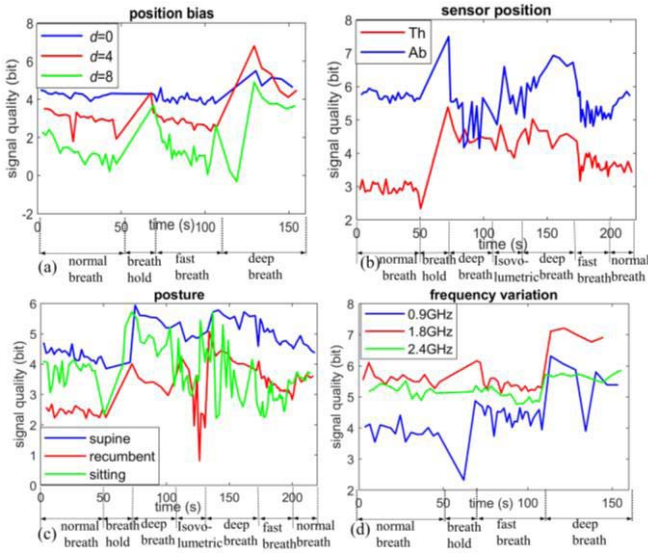


Fig. 8. Signal quality for (a) Position variation: $d = 0$ (green), 4 ins (red), and 8 ins (blue); (b) Sensor placement: thorax (blue) and abdomen (red); (c) Postures: sitting (red), supine (green), and recumbent (blue); (d) Carrier frequency: $f_{RF} = 0.9$ GHz (blue), 1.8 GHz (red), and 2.4 GHz (green).

TABLE II
SNR CALCULATED IN DIFFERENT CONDITIONS

(a) Position bias	SNR (dB)	(b) Sensor placement	SNR (dB)
$d = 0$	16.2	Supine thorax	10.7
$d = 4$ in	6.60	Supine abdomen	14.3
$d = 8$ in	5.92		
(c) Posture	SNR (dB)	(d) Frequency	SNR (dB)
Supine	19.3	0.9GHz	8.41
Recumbent	14.6	1.8GHz	12.2
Sitting	8.05	2.4GHz	9.69

abdomen sensors in Fig. 8(b) when they operated together in the supine position with $f_{RF} = 2.4$ GHz. Abdomen often has larger motion from the diaphragm and associated muscles, and overall larger Q . Using measurements in Fig. 8(c), we compared Q in the supine, recumbent, and sitting postures from the abdomen sensor with $f_{RF} = 1.8$ GHz. The supine signal has larger Q than those by recumbent and sitting due to higher coupling strength between the RF signal and the body. Finally, for frequency variation in Fig. 8(d) at $f_{RF} = 0.9$, 1.8, and 2.4 GHz, we used the abdomen sensor in the supine position for illustration. Q has a more complex relation with respect to f_{RF} , although 1.8 GHz usually performed the best. All frequencies can be employed to retrieve respiration waveforms, but different Tx and Rx gains need to be chosen in our adaptive-gain implementation in SDR.

The corresponding SNRs calculated in different conditions in Fig. 8 are shown in Table II. SNR is calculated during the normal breathing period of 0 – 50s when BR is roughly constant. The comparison of SNR under different conditions show similar trends to Q in our controlled ambient without additional interferences.

G. Comparison With Antenna-Based NCS Sensors

We also compared the performance of the notched NCS sensor and the wearable antenna-based NCS sensor [26].

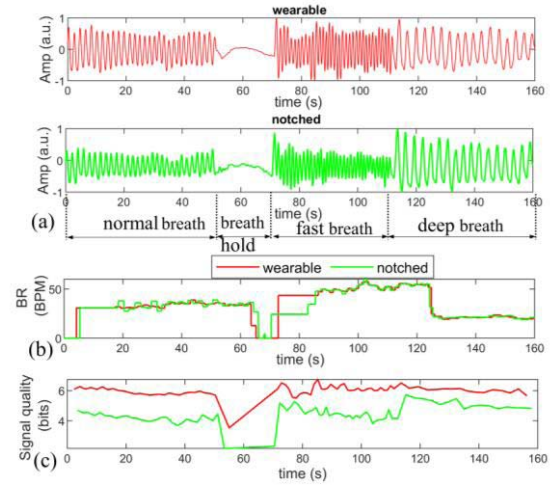


Fig. 9. (a) Waveforms of the wearable sensor (red) and the notched sensor (green) both at the abdomen position. (b)(c) The corresponding estimated BR and Q .

The wearable sensor consists of ultra-high frequency (UHF) monopole antennas used at both Tx and Rx. Two wearable sensors were separately attached to the thorax and abdomen in the front torso in the similar location of the BIOPAC chest belts. Two notched sensors were integrated to the chair setup in the back. One SDR by B210 was connected to two notched sensors and another B210 was connected to two wearable sensors. f_{RF} was set at 1.8 GHz. The breathing protocol was the same as in Fig. 5. In Fig. 9(a), we demonstrated the waveforms of the wearable sensor (red) and the notched sensor (green) both at the abdomen position. In Figs. 9(b)(c), the corresponding BR and Q were extracted. BR from the two sensors are well matched, but the wearable sensors have a higher Q indicating better coupling strength than the notched sensor. This is reasonable because the wearable sensors were more closely attached to the body in the front torso. Also, the wearable sensors are monopole antennas with intentional radiation into the body, but the notched sensors depend only on near-field leakage by the evanescent mode.

H. Two-Tone Measurements

We also confirmed the two-tone measurement capability in the notched sensor, which can enhance reliability by frequency diversity. Different f_{RF} will have different body penetration depth, as indicated in the CST simulation of Supplementary Fig. 1(b). In comparison with the antenna-based NCS systems, dual-band antennas are more complicated to design, especially in the consideration of body antenna detuning. For the notched sensor, two f_{RF} can be applied simultaneously to one sensor, and one or two f_{RF} can be applied to two collocated cables with reasonable spatial isolation. In Fig. 10, two-tone Strategy 1 has a frequency multiplexing setup by two SDRs feeding into the same RF cable at the same time. Broadband 3dB splitters are utilized to combine two RF signals into one notched sensor and then splitting back to the Rx of the respective carrier. Two-tone Strategy 2 has two closely collocated notched cables. Two SDRs with different

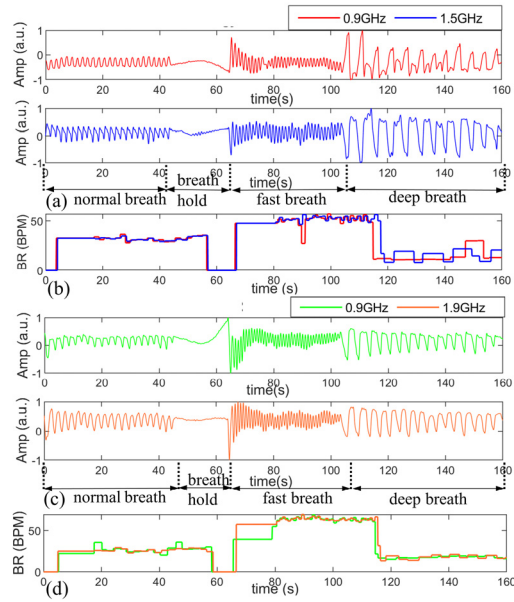


Fig. 10. (a) Two-tone Strategy 1: Respiration waveforms for 0.9 GHz (upper) and 1.5 GHz (lower); (b) The corresponding BR estimation. (c) Two-tone Strategy 2: Respiration waveforms for 0.9 GHz (upper) and 1.9 GHz (lower); (d) the corresponding BR estimation.

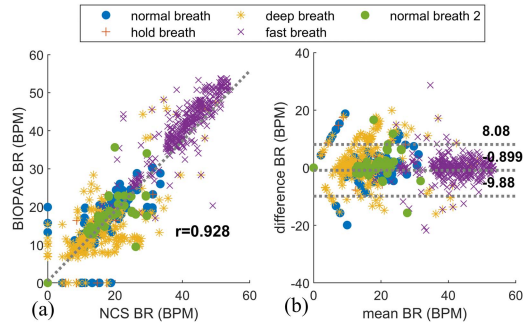


Fig. 11. Correlation and agreement between NCS and BIOPAC BR data from 10 participants. (a): The scatter plot with denoted Pearson's correlation coefficient. (b): The Bland-Altman plot.

frequencies separately fed into two notched sensors. At the same position, we have two sensors by two f_{RF} with minimal interference to each other.

The 160-s protocol was the same as Fig. 4 for position variation testing in the supine posture with the abdomen sensor. In Figs. 10(a)(b), Strategy 1 of frequency multiplexing has f_{RF} at 0.9 GHz and 1.5 GHz. In Figs. 10(c)(d), Strategy 2 of the collocated sensor cables has f_{RF} at 0.9 GHz and 1.9 GHz. BR extracted from different f_{RF} is consistent for both strategies. Notice that the two-tone measurements can be employed for signal quality check or for coupling into different body depth. Optimal choices of multiple f_{RF} in different scenarios will need further study.

I. Validation on Multiple Participants

Finally, we have validated our system on 10 different participants. The routine was the same as that in Fig. 3 with the notched sensors on bed and commercial torso-belt sensors on

TABLE III
CORRELATION AND B&A STATISTICS FOR EACH PARTICIPANT

Case No.	r	m (RPM)	σ (RPM)
1	0.927	-1.65	4.50
2	0.987	0.586	2.24
3	0.951	-0.465	4.36
4	0.999	-0.0103	0.288
5	0.978	-0.210	2.12
6	0.805	-4.81	7.13
7	0.883	0.552	5.37
8	0.954	-0.631	4.22
9	0.955	0.131	3.27
10	0.913	-1.24	5.62

the user body. The retrieved BR from 10 participants compare well with the synchronous chest-belt sensors in all breathing routines. The correlation and agreement plots between NCS and BIOPAC BR data of all 10 people are shown in Fig. 11. The correlation and B&A statistics of individual participants are shown in Table III. The isovolumetric exercise detection statistics of each participant were recorded in Supplementary Table II. Also, the body characteristics of each participant are recorded in Supplementary Table IV. For most cases, the correlation is relatively high, m is low and LoA is narrow. Only a small number of cases have a relatively lower correlation. Our present sample size is too small to draw reliable conclusion on the effects from body characteristics. However, it remains safe to say that the NCS system can accurately detect BR on different people, demonstrating high consistency with commercial torso-belt sensors.

IV. CONCLUSION

In this article, a new notched-cable sensor based on NCS for respiration monitoring was demonstrated. The sensor was integrated to a bed and a chair under layers of fabrics, and is hence highly comfortable, stable, accurate, and cost-effective. In comparison with the wearable sensors attached to the body, our system is invisible to the user with the least concerns of comfort and conspicuousness. Confirmed by experiments, our system has the following advantages: 1) Tolerance of large position variation to accommodate user uncertainty; 2) Posture applicability including supine and recumbent on bed, as well as sitting on chair; 3) Availability of HR estimation in one setup; 4) Identification of multiple breathing patterns including deep, fast, tidal, held and blocked breathing; 5) Broad bandwidth of operations to facilitate multiplexing and signal quality improvement in different scenarios.

There are still remaining issues for future work. The accuracy of paradoxical motion detection during isovolumetric exercise should be further improved. Also, larger variation on people size, body figure and breathing habits should be included in broader user study to further establish heuristic improvement from known body characteristics.

REFERENCES

- [1] C. Massaroni, A. Nicolò, D. Lo Presti, M. Sacchetti, S. Silvestri, and E. Schena, "Contact-based methods for measuring respiratory rate," *Sensors*, vol. 19, no. 4, p. 908, Feb. 2019, doi: 10.3390/s19040908.

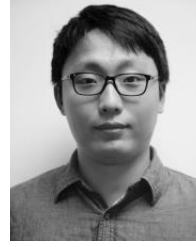
- [2] D. Oletic and V. Bilas, "Energy-efficient respiratory sounds sensing for personal mobile asthma monitoring," *IEEE Sensors J.*, vol. 16, no. 23, pp. 8295–8303, Dec. 2016, doi: [10.1109/jsen.2016.2585039](https://doi.org/10.1109/jsen.2016.2585039).
- [3] D. Naranjo-Hernández *et al.*, "Smart vest for respiratory rate monitoring of COPD patients based on non-contact capacitive sensing," *Sensors*, vol. 18, no. 7, p. 2144, Jul. 2018, doi: [10.3390/s18072144](https://doi.org/10.3390/s18072144).
- [4] O. Oldenburg, B. Lamp, L. Faber, H. Teschl, D. Horstkotte, and V. Töpfer, "Sleep-disordered breathing in patients with symptomatic heart failure a contemporary study of prevalence in and characteristics of 700 patients," *Eur. J. Heart Failure*, vol. 9, no. 3, pp. 251–257, Mar. 2007, doi: [10.1016/j.ejheart.2006.08.003](https://doi.org/10.1016/j.ejheart.2006.08.003).
- [5] M. A. Cretikos, R. Bellomo, K. Hillman, J. Chen, S. Finfer, and A. Flabouris, "Respiratory rate: The neglected vital sign," *Med. J. Aust.*, vol. 188, no. 11, pp. 657–659, Jun. 2008.
- [6] P. Barthel *et al.*, "Respiratory rate predicts outcome after acute myocardial infarction: A prospective cohort study," *Eur. Heart J.*, vol. 34, no. 22, pp. 1644–1650, Jun. 2013, doi: [10.1093/europress/ehs420](https://doi.org/10.1093/europress/ehs420).
- [7] M. Grassmann, E. Vlemincx, A. von Leupoldt, J. M. Mittelstädt, and O. Van den Berghe, "Respiratory changes in response to cognitive load: A systematic review," *Neural Plasticity*, vol. 2016, pp. 1–16, Jun. 2016, doi: [10.1155/2016/8146809](https://doi.org/10.1155/2016/8146809).
- [8] A. Nicolò, C. Massaroni, and L. Passfield, "Respiratory frequency during exercise: The neglected physiological measure," *Frontiers Physiol.*, vol. 8, p. 922, Dec. 2017, doi: [10.3389/fphys.2017.00922](https://doi.org/10.3389/fphys.2017.00922).
- [9] W. J. DePaso, R. H. Winterbauer, J. A. Lusk, D. P. Dreis, and S. C. Springmeyer, "Chronic dyspnea unexplained by history, physical examination, chest roentgenogram, and spirometry," *Chest*, vol. 100, no. 5, pp. 1293–1299, Nov. 1991, doi: [10.1378/chest.100.5.1293](https://doi.org/10.1378/chest.100.5.1293).
- [10] F. Q. Al-Khalidi, R. Saatchi, D. Burke, H. Elphick, and S. Tan, "Respiration rate monitoring methods: A review," *Pediatric Pulmonol.*, vol. 46, no. 6, pp. 523–529, Jun. 2011, doi: [10.1002/ppul.21416](https://doi.org/10.1002/ppul.21416).
- [11] A. Abid, R. J. Mieloszyk, G. C. Verghese, B. S. Krauss, and T. Heldt, "Model-based estimation of respiratory parameters from capnography, with application to diagnosing obstructive lung disease," *IEEE Trans. Biomed. Eng.*, vol. 64, no. 12, pp. 2957–2967, Dec. 2017.
- [12] S. Gong *et al.*, "A wearable and highly sensitive pressure sensor with ultrathin gold nanowires," *Nature Commun.*, vol. 5, no. 1, pp. 1–8, Feb. 2014, doi: [10.1038/ncomms4132](https://doi.org/10.1038/ncomms4132).
- [13] S. Stick, E. Ellis, P. LeSouëf, and P. Sly, "Validation of respiratory inductance plethysmography ('Respirtrace') for the measurement of tidal breathing parameters in newborns," *Pediatric Pulmonol.*, vol. 14, no. 3, pp. 187–191, Nov. 1992.
- [14] N. Netzer, A. H. Eliasson, C. Netzer, and D. A. Kristo, "Overnight pulse oximetry for sleep-disordered breathing in adults," *Chest*, vol. 120, no. 2, pp. 625–633, Aug. 2001.
- [15] E. Nemati, M. Deen, and T. Mondal, "A wireless wearable ECG sensor for long-term applications," *IEEE Commun. Mag.*, vol. 50, no. 1, pp. 36–43, Jan. 2012.
- [16] B. A. Reyes, N. Reljin, Y. Kong, Y. Nam, and K. H. Chon, "Tidal volume and instantaneous respiration rate estimation using a volumetric surrogate signal acquired via a smartphone camera," *IEEE J. Biomed. Health Informat.*, vol. 21, no. 3, pp. 764–777, May 2017, doi: [10.1109/JBHI.2016.2532876](https://doi.org/10.1109/JBHI.2016.2532876).
- [17] C. Li, V. M. Lubecke, O. Boric-Lubecke, and J. Lin, "A review on recent advances in Doppler radar sensors for noncontact healthcare monitoring," *IEEE Trans. Microw. Theory Techn.*, vol. 61, no. 5, pp. 2046–2060, May 2013, doi: [10.1109/tmtt.2013.2256924](https://doi.org/10.1109/tmtt.2013.2256924).
- [18] K. S. Park, S. H. Hwang, H. N. Yoon, and W. K. Lee, "Ballistocardiography for nonintrusive sleep structure estimation," in *Proc. Conf. 36th IEEE Eng. Med. Biol. Soc.*, Aug. 2014, pp. 5184–5187.
- [19] C. Song and P. Wang, "A radio frequency device for measurement of minute dielectric property changes in microfluidic channels," *Appl. Phys. Lett.*, vol. 94, no. 2, Jan. 2009, Art. no. 023901.
- [20] J. Naqui and F. Martin, "Transmission lines loaded with bisymmetric resonators and their application to angular displacement and velocity sensors," *IEEE Trans. Microw. Theory Techn.*, vol. 61, no. 12, pp. 4700–4713, Dec. 2013, doi: [10.1109/tmtt.2013.2285356](https://doi.org/10.1109/tmtt.2013.2285356).
- [21] A. Ebrahimi, J. Scott, and K. Ghorbani, "Differential sensors using microstrip lines loaded with two split-ring resonators," *IEEE Sensors J.*, vol. 18, no. 14, pp. 5786–5793, Jul. 2018, doi: [10.1109/jsen.2018.2840691](https://doi.org/10.1109/jsen.2018.2840691).
- [22] S. Harnsoongnoen and A. Wanthong, "Coplanar waveguide transmission line loaded with electric-LC resonator for determination of glucose concentration sensing," *IEEE Sensors J.*, vol. 17, no. 6, pp. 1635–1640, Mar. 2017, doi: [10.1109/jsen.2017.2652121](https://doi.org/10.1109/jsen.2017.2652121).
- [23] X. Hui and E. C. Kan, "Monitoring vital signs over multiplexed radio by near-field coherent sensing," *Nature Electron.*, vol. 1, no. 1, pp. 74–78, Jan. 2018, doi: [10.1038/s41928-017-0001-0](https://doi.org/10.1038/s41928-017-0001-0).
- [24] CST Microwave Studio. (2020). *Computer Simulation Technology*. [Online]. Available: <http://www.cst.com>
- [25] P. Sharma and E. C. Kan, "Sleep scoring with a UHF RFID tag by near field coherent sensing," in *IEEE MTT-S Int. Microw. Symp. Dig.*, Philadelphia, PA, USA, Jun. 2018, pp. 1419–1422.
- [26] P. Sharma, X. Hui, and E. C. Kan, "A wearable RF sensor for monitoring respiratory patterns," in *Proc. 41st Annu. Int. Conf. IEEE Eng. Med. Biol. Soc. (EMBC)*, vol. 27, Jul. 2019, pp. 1217–1223.
- [27] R. M. Fano, "Theoretical limitations on the broadband matching of arbitrary impedances," *J. Franklin Inst.*, vol. 249, no. 1, pp. 57–83, Jan. 1950.
- [28] W. Lu *et al.*, "A semi-automatic method for peak and valley detection in free-breathing respiratory waveforms," *Med. Phys.*, vol. 33, no. 10, pp. 3634–3636, Oct. 2006, doi: [10.1118/1.2348764](https://doi.org/10.1118/1.2348764).
- [29] P. Sharma, X. Hui, J. Zhou, T. B. Conroy, and E. C. Kan, "Wearable radio-frequency sensing of respiratory rate, respiratory volume, and heart rate," *NJP Digit. Med.*, vol. 3, no. 1, pp. 1–10, Dec. 2020, doi: [10.1038/s41746-020-0307-6](https://doi.org/10.1038/s41746-020-0307-6).



Zijing Zhang received the B.Eng. degree in optoelectronic engineering from the Huazhong University of Science and Technology (HUST), Wuhan, China, in 2019. She is currently pursuing the Ph.D. degree in electrical engineering with Cornell University, Ithaca, NY, USA.



Pragya Sharma (Member, IEEE) received the B.Tech. degree in electrical engineering from the Indian Institute of Technology Kharagpur (IIT Kharagpur), Kharagpur, India, in 2015. She is currently pursuing the Ph.D. degree in electrical engineering with Cornell University, Ithaca, NY, USA.



Jianlin Zhou received the B.S. degree in electronics and information engineering from the Nanjing University of Science and Technology, Nanjing, China, in 2013, and the M.S. degree in electrical and computer engineering from Northeastern University, Boston, MA, USA, in 2016. He is currently pursuing the Ph.D. degree in electrical and computer engineering with Cornell University, Ithaca, NY, USA. He has previously worked as a Research Support Associate on ingestible electronics design for drug delivery and bio-sensing at the Robert Langer Lab, Massachusetts Institute of Technology from 2016 to 2018.



Xiaonan Hui (Member, IEEE) received the B.S. degree from Northeastern University, China, in 2012, and the M.S. degree from Zhejiang University, China, in 2015, all in electrical engineering. He is currently pursuing the Ph.D. degree in electrical and computer engineering with Cornell University, Ithaca, NY, USA.



Edwin C. Kan (Senior Member, IEEE) received the B.S. degree from National Taiwan University in 1984 and the M.S. and Ph.D. degrees from the University of Illinois at Urbana-Champaign in 1988 and 1992, respectively, all in electrical engineering. From 1984 to 1986, he has served in the Air Force, Taiwan, R.O.C., as a Second Lieutenant. In January 1992, he joined Dawn Technologies Corporation as a Principal CAD Engineer. He was a Research Associate with Stanford University from 1994 to 1997. In 1997, he joined the School of Electrical and Computer Engineering, Cornell University, Ithaca, NY, USA, as an Assistant Professor, where he is a Professor.